Tellus (1998), 50A, 242–257
Printed in UK – all rights reserved

TELLUS
ISSN 0280–6495

Numerical experiments with a fluid heated non-uniformly from below

By T. ROSSBY, *Graduate School of Oceanography, University of Rhode Island, Kingston, RI 02881, USA*

(Manuscript received 4 April 1997; in final form 24 October 1997)

ABSTRACT

Convection in a square container driven by non-uniform heating from below is investigated. It is shown that the normalized heat transport, the Nusselt number (Nu), obeys an $Ra^{1/5}$ power law where Ra is the Rayleigh number based on the total temperature contrast along the bottom. As the Prandtl number (Pr) is decreased from 10 to 1 ($Ra > 10^6$), the stream function increases rapidly while Nu decreases. For a given Ra, Nu is a strong function of the shape of the imposed temperature distribution and increases as the lateral extent of the thermal contrast is reduced. It is also shown that the response of the system to a new temperature distribution is slow or rapid depending upon whether or not the interior temperature field is affected. These experiments re-emphasize what is sometimes overlooked, namely that the thermohaline circulation is driven by the imposed horizontal (meridional density) contrast and not by the deep convection per se.

1. Introduction

Dense water is supplied to the deep ocean by surface cooling in two limited areas, the Greenland and Labrador Seas in the north, and the Weddell Sea in the south. These waters spread out into all ocean basins and slowly upwell towards the surface as they are replaced by new deep waters. While production of deep waters occurs every winter the time scale for the overturning is on the order of 1000 years. This extreme asymmetry of sinking and upwelling was addressed by Stommel (1962) in a simple yet instructive study. Using a model consisting of an array of vertical pipes, all connected to a deep reservoir at the lower end and connected to a single horizontal pipe at the top with a distributed temperature profile, he was able to demonstrate the asymmetry of vertical motion: sinking occurred only in one pipe at the cold end while in all other pipes water slowly rose and warmed through conduction.

At Stommel's initiative, a laboratory experiment was undertaken to test the predictions of the pipe model. A fluid in a rectangular container, insulated on the sides and top, was subject to a linear temperature profile along the bottom. The resulting density difference in the fluid next to the bottom forced a rapid flow from the cold end to the warm where it rose in a narrow plume. From there, the fluid spread out across the tank and slowly returned back towards the bottom (Rossby, 1965, hereafter R65). The asymmetric shape of the convection cell was attributed to the inefficiency of conduction compared to that of advection. A corollary result was that the narrowness of the convecting fluid was insensitive to the shape of the applied temperature distribution, though, in fact, the latter was not varied.

A scale analysis of the experiments (R65) suggested that the Nusselt number (Nu), which is the ratio of total heat fluxes with and without fluid motion, should increase as the Rayleigh number (Ra) to the one-fifth power where $Ra = \alpha g \Delta T L^3/\nu\kappa$ is based on the applied temperature difference ΔT and length L of the container. α, κ and ν are the coefficients of thermal expansion, thermal diffusivity and kinematic viscosity respectively, and g denotes gravity. While the scale analysis seemed to account for the experimental results, it was necessary for experimental reasons to vary the viscosity (ν) of the fluid instead of temperature to achieve a wide range of Ra. The same scale analysis indicated that there should be little Prandtl number ($\mathrm{Pr} = \nu/\kappa$) dependence (for large Pr), but this assumption was not verified. In addition, the analysis indicated that the boundary layer should scale as $\mathrm{LRa}^{-1/5}$.

Several numerical studies of a fluid driven by non-uniform temperature distributions confirmed the asymmetric shape of the convecting cell (Barcilon and Veronis, 1965 (unpublished manuscript); Somerville, 1967; Beardsley and Festa, 1972). However, machine limitations and cost of numerical modelling at the time restricted these studies to modest Ra compared to the much higher Ra at which the experiments were done and thus could not test the results of the scale analysis. Nonetheless, all studies confirmed the observation that heat enters the interior in a narrow ascending jet and is removed by conduction across a narrow thermal boundary layer at the bottom.

Stommel (1962) and R65 pointed out that the asymmetry of the convecting cell was insensitive to the shape of the imposed temperature distribution, but little was noted about the strength of the convection. For a given total temperature difference, one can anticipate that the convection will be stronger as the lateral extent of the temperature contrast is limited towards the center. In geophysical terms this would be as if the imposed meridional temperature gradient was limited to mid-latitudes (perhaps the result of a stable zonal circulation in the atmosphere), or pushed to low and high latitudes due to an energetic mesoscale in the atmosphere at mid-latitudes. Thus the inhibition of meridional exchange in the atmosphere due to a stable zonal jet would strengthen the imposed temperature contrast on the ocean and hence its rate of overturning, and vice versa. How sensitive is the heat flux to the shape of the imposed temperature distribution?

In this study, we use the numerical framework developed by Beardsley and Festa (1972, hereafter BF72) to test the scale analysis over a much wider range of Ra than was possible at that time. To verify the Pr independence assumption several experiments are conducted for Pr between 1 and 100 at both low and high Ra. We then examine the sensitivity of the convection to departures from a linear temperature distribution. Lastly we briefly consider the effect of a forced flow, expressed in terms of a transport, in and out of the bottom boundary, as a non-rotating anologue of Ekman pumping.

The major result of this study is to confirm the earlier scale analysis, namely that Nu and the streamfunction maximum follow the $\mathrm{Ra}^{1/5}$ scaling quite accurately provided that $\mathrm{Pr} \gg 1$. Also consistent with the earlier experimental work, the mean temperature of the fluid is all but independent of Ra, but is significantly affected by the shape of the imposed temperature distribution. Experiments with different temperature distributions along the boundary reveal markedly different response times depending on where the temperature change is imposed. At large Ra ($>10^6$), a striking Pr dependence develops for $\mathrm{Pr} < 10$: the stream function increases rapidly while the Nusselt number decreases as Pr is decreased.

2. The model

We consider a fluid in a square container insulated on all sides except the bottom along which a certain temperature distribution is imposed. Following R65 and BF72, the governing equations are the vorticity equation

$$\frac{\partial \eta}{\partial t} - J(\Psi, \eta) = \upsilon \nabla^2 \eta - \alpha g T_x \,, \tag{1}$$

and the heat equation

$$\frac{\partial T}{\partial t} = J(\Psi, T) + \kappa \nabla^2 T \,, \tag{2}$$

where Ψ is the streamfunction, $\eta = \nabla^2 \Psi$ is the vorticity and T is the temperature. J(-,-) is the Jacobian and ∇^2 is the Laplacian operator. In all studies (except when we consider Ekman-like pumping at the bottom) we assume no normal flow and free-slip conditions on all sides, i.e. $\Psi = 0$ and $\partial^2 \Psi / \partial n^2 = 0$. This last condition differs from

BF72 who assumed no-slip conditions on the sides and top, and free-slip at the bottom.

This system is readily non-dimensionalized to become

$$\frac{\partial \eta}{\partial t} = J(\Psi, \eta) + \mathrm{Pr}\left(-Ra\frac{\partial T}{\partial x} + \nabla^2 \eta\right), \tag{3}$$

$$\frac{\partial T}{\partial t} = J(\Psi, T) + \nabla^2 T\,. \tag{4}$$

where $\mathrm{Ra} = \alpha g \Delta T L^3/\nu\kappa$, $\mathrm{Pr} = \nu/\kappa$, and L is the size of the square vessel.

The numerical formulation of the problem follows BF72 closely. We assume a square grid with a resolution that can be adjusted depending upon the strength of the circulation. The Jacobians use the J_2 and J_3 Arakawa schemes for the advection of heat and vorticity. The Laplacians are represented by the standard five-point scheme. The time steps are approximated by a standard time-centered scheme. The resulting finite-difference formulation is the same as that of BF72:

$$\begin{aligned}\frac{\eta_{ij}^{n+1} - \eta_{ij}^{n-1}}{2\Delta t} = \frac{J_3(\Psi^n, \eta^n)}{4\delta^2} &- \frac{\mathrm{Pr}\, Ra}{2\delta}(T_{i+1j}^n - T_{i-1j}^n)\\ &+ \frac{\mathrm{Pr}}{\delta^2}(\eta_{i+1j}^n + \eta_{i+1j}^n + \eta_{ij+1}^n\\ &+ \eta_{ij-1}^n - 2\eta_{ij}^{n+1} - 2\eta_{ij}^{n-1}),\end{aligned} \tag{5}$$

$$\begin{aligned}\frac{T_{ij}^{n+1} - T_{ij}^{n-1}}{2\Delta t} = \frac{J_2(\Psi^n, T^n)}{4\delta^2} &+ \frac{1}{\delta^2}(T_{i+1j}^n + T_{i-1j}^n\\ &+ T_{ij+1}^n + T_{ij-1}^n - 2T_{ij}^{n+1} - 2T_{ij}^{n-1}).\end{aligned} \tag{6}$$

The streamfunction Ψ^{n+1} is computed from the updated vorticity field η_{ij}^{n+1} from the Poisson equation:

$$\eta_{ij}^{n+1} = \frac{1}{\delta^2}(\Psi_{i+1j}^{n+1} + \Psi_{i-1j}^{n+1} + \Psi_{ij+1}^{n+1} + \Psi_{ij-1}^{n+1} - 4\Psi_{ij}^{n+1}). \tag{7}$$

Unlike BF72 who use an alternating-direction-implicit scheme, we transform (7) into wave-number space using only sine functions which automatically satisfy the boundary conditions for the streamfunction field (Press et al., 1986). We write Ψij as

$$\Psi_{ij} = \frac{4}{(M+1)(N+1)}\sum_{m=1}^{M}\sum_{n=1}^{N}\Phi_{mn} \times \sin\frac{im\pi}{M+1}\sin\frac{jn\pi}{N+1}, \tag{8}$$

where Φ_{mn} is the Fourier transform of Ψ_{ij}:

$$\Phi_{mn} = \sum_{i=1}^{M}\sum_{j=1}^{N}\Psi_{ij}\sin\frac{im\pi}{M+1}\sin\frac{jn\pi}{N+1}. \tag{9}$$

Inserting (8) into (7) and taking advantages of certain symmetries, writing the Fourier transform of η as N, we obtain

$$\Phi_{mn} = \frac{N\delta^2}{2\left(\cos\left(\frac{m\pi}{M+1}\right) + \cos\left(\frac{n\pi}{N+1}\right)\right) - 4}. \tag{10}$$

Inserting this back into (8) the streamfunction Ψ_{ij}^{n+1} is obtained. By precomputing all the trigonometric coefficients, the transformations are reduced to algebraic sums.

Computational stability was ensured by making sure that the time step δT satisfied the Courant-Friedrichs-Lewy condition that $U_{\max}\delta T/\delta < 1$ where $U_{\max}$ is the maximum speed in the fluid and δ is the grid spacing. Validation of the results was done by comparing the computed fields at different resolution levels and by approaching equilibrium from different initial conditions.

Using the computed fields, the principal objective of the simulations was to determine the strength of the circulation and Nu, the Nusselt number. The total heat flux is estimated from

$$H = \frac{1}{2}\int_0^1 |(T_y)_{y=0}|\,\mathrm{d}x\,, \tag{11}$$

where $(T_y)_{y=0}$ is determined from a Taylor series expansion of temperature at the bottom:

$$(T_y)_{y=0} = (-1.5T_j + 2T_{j+1} - 0.5T_{j+2})/\delta \quad (j=1). \tag{12}$$

The Nusselt number is defined as H in (11) divided by the same quantity in the absence of any motion (conduction only). A measure of equilbrium is when the net heat flux $\int_0^1 (T_y)_{y=0}\mathrm{d}x$ into the fluid approaches zero; in practice this was usually between $+3$ and $+6\%$ of H, but in a few cases at low Pr, a larger error was tolerated. The positive errors mean that more heat appears to be entering than leaving the fluid.

3. Results

3.1. *Thermal convection with linear temperature distribution*

The fluid in these experiments was driven with a linear temperature profile imposed at the bottom. Since the strength of the forcing was expressed through Ra, the non-dimensional temperature is always 0 to 1 from cold to warm. Most experiments were run with the $\mathrm{Pr} = 10$, but, as we shall see, starting at $\mathrm{Ra} \approx 10^5$ there was noticeable Pr dependence. For all Ra considered here ($\leqslant 10^8$), steady convection was possible. In most cases the solutions for a given Ra were started from a lower Ra and run to a new equilibrium. In some cases the resulting fields were interpolated onto a finer grid and rerun until steady state conditions were met, defined as when the heat flux error was within one percent of its asymptotic limit.

The stream function is contoured for six Ra in Fig. 1. As Ra is increased, the circulation increases and the center of the cell moves down reflecting the increasing gradients at the bottom. At higher Ra the eye or center of the convection cell is pushed to the right and a boundary layer along the right wall is established. The boundary layer flow along the bottom then continues as an ascending jet or plume along the right wall with a return flow to the interior at all heights. For $\mathrm{Ra} > 10^7$ there is clear tendency for the jet to continue to the top and form a boundary layer there as well. In addition, the center of the vortex becomes increasingly elongated and by $\mathrm{Ra} = 10^8$ has split into two maxima.

The corresponding temperature distributions are shown in Fig. 2. As Ra is increased the boundary layer gradually decreases in thickness. The contour interval is 0.1; in addition between temperatures 0.7 and 0.8 isotherms are dashed for every 0.01 units to indicate the near uniformity of temperature in the interior of the container. The streamfunction maximum (Ψ_{max}) and Nu are plotted as a function of Ra in Fig. 3 (left panel). The Nu results can be summarized quite effectively with a one-fifth power law, $\mathrm{Nu} = 0.35x\mathrm{Ra}^{1/5}$ (dashed line), even at low Ra when the convection is still quite weak. The reason appears to be that even for weak convection where the increase in heat flux is still quite modest, the isotherms are distorted from the purely conductive state into thermal boundary layers. The right panel shows the same Nu results together with the observed values reported by R65. In the experiments Pr decreased from a high of 8500 at $\mathrm{Ra} = 1.1 \times 10^7$ to 13 at $\mathrm{Ra} = 1.6 \times 10^{10}$. (The Rayleigh number was increased by choosing a Silicone oil of lower viscosity.)

A power law relationship does not emerge for Ψ_{max} until much higher Ra ($> 10^5$), beyond which it appears to asymptote to a 1/5-law. The experiments are summarized in Table 1, which also includes the mean temperature of the fluid and the temperature at the eye of the vortex, both of which increase only slightly as Ra is increased. As noted by BF72, these two temperatures track each other very closely.

The Pr-independence suggested by the R65 study was restricted to large Pr. In these calculations, we have used $\mathrm{Pr} = 10$, which is considerably less than that of the oils used in R65. To verify the Pr-independence further, we estimate Nu and Ψ_{max} between $10^5 \leqslant \mathrm{Ra} \leqslant 10^8$ and $1 \leqslant \mathrm{Pr} \leqslant 100$. The results are summarized in Fig. 4, Table 2. The left panel in Fig. 4 shows Ψ_{max} as a function of Ra for $\mathrm{Pr} = 1$, 3, 10, 100 normalized by the stream function at $\mathrm{Pr} = 100$. The right panel shows the corresponding normalized Nu. For $\mathrm{Ra} > 10^7$, as Pr is decreased, Ψ_{max} increases rapidly although at $\mathrm{Ra} = 10^8$, it decreases slightly at $\mathrm{Pr} = 10$ before

Table 1. *Summary of experiments with a linear temperature distribution ($Pr = 10$)*

Ra	Ψ_{max}	Nu	$\langle T \rangle$	T_{eye}	N	% err
10^3	0.92	1.11	0.56	0.56	41	2.2
3×10^3	1.99	1.38	0.608	0.604	41	3.1
10^4	3.77	1.88	0.648	0.644	41	3.3
3×10^4	6.09	2.47	0.671	0.671	41	3.6
10^5	9.40	3.24	0.700	0.695	61	3.4
3×10^5	14.1	4.18	0.706	0.705	61	6.2
10^6	19.1	5.36	0.723	0.713	61	5.1
3×10^6	26.3	6.80	0.722	0.716	61	6.3
10^7	32.5	8.63	0.741	0.719	81	7.8
3×10^7	42.7	10.8	0.736	0.719	81	6.8
10^8	55.7	13.8	0.735	0.719	101	5.1

The 6 panels in Figs. 1, 2 correspond to $\mathrm{Ra} = 10^3$, 10^4, 10^5, 10^6, 10^7, 10^8, respectively.

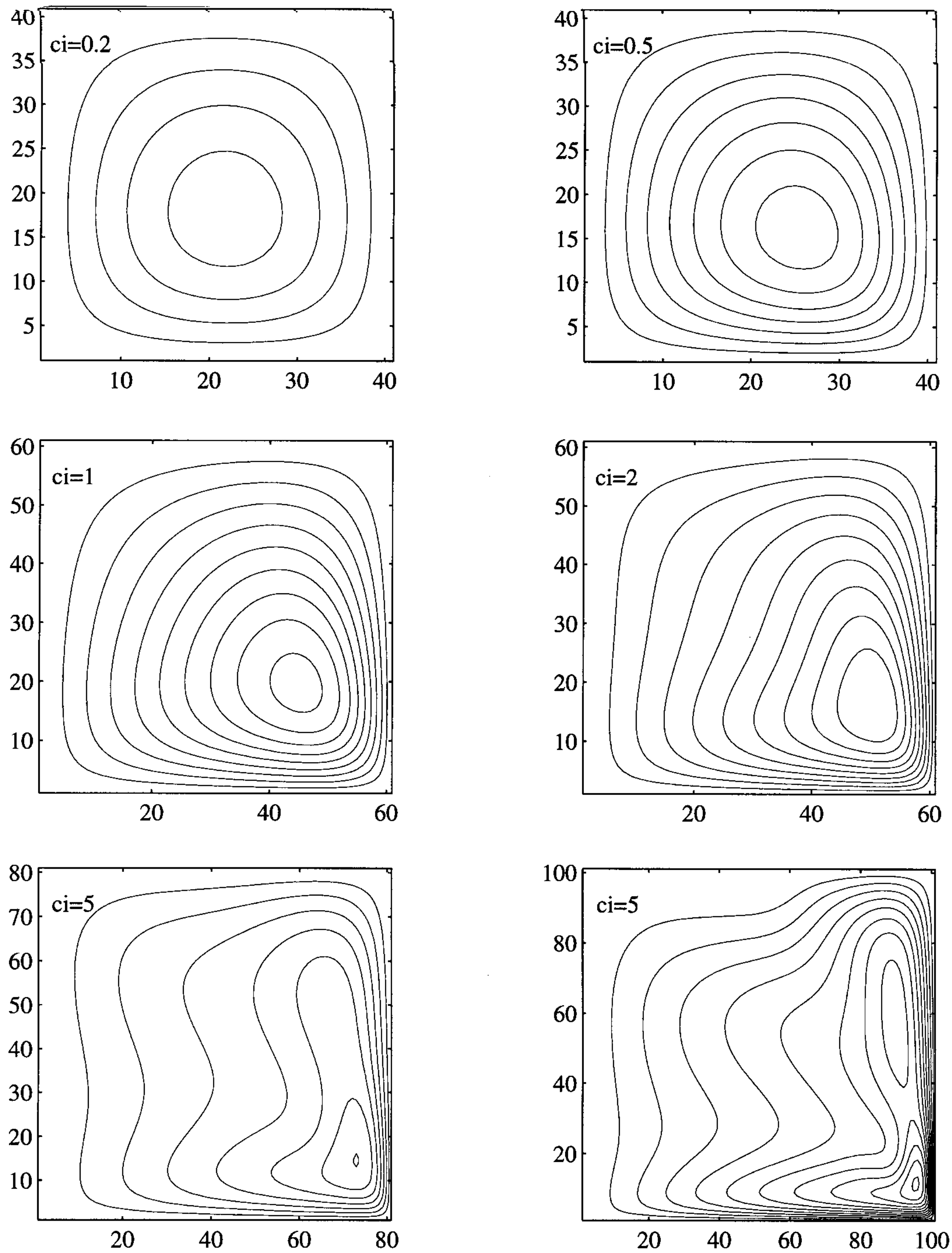

Fig. 1. $\Psi(x, y)$ at Rayleigh numbers 10^3, 10^4, 10^5, 10^6, 10^7, 10^8 (left to right, top to bottom). The axes indicate the number of grid points in the horizontal vertical. ci refers to the contour interval used. See Table 1 for further details.

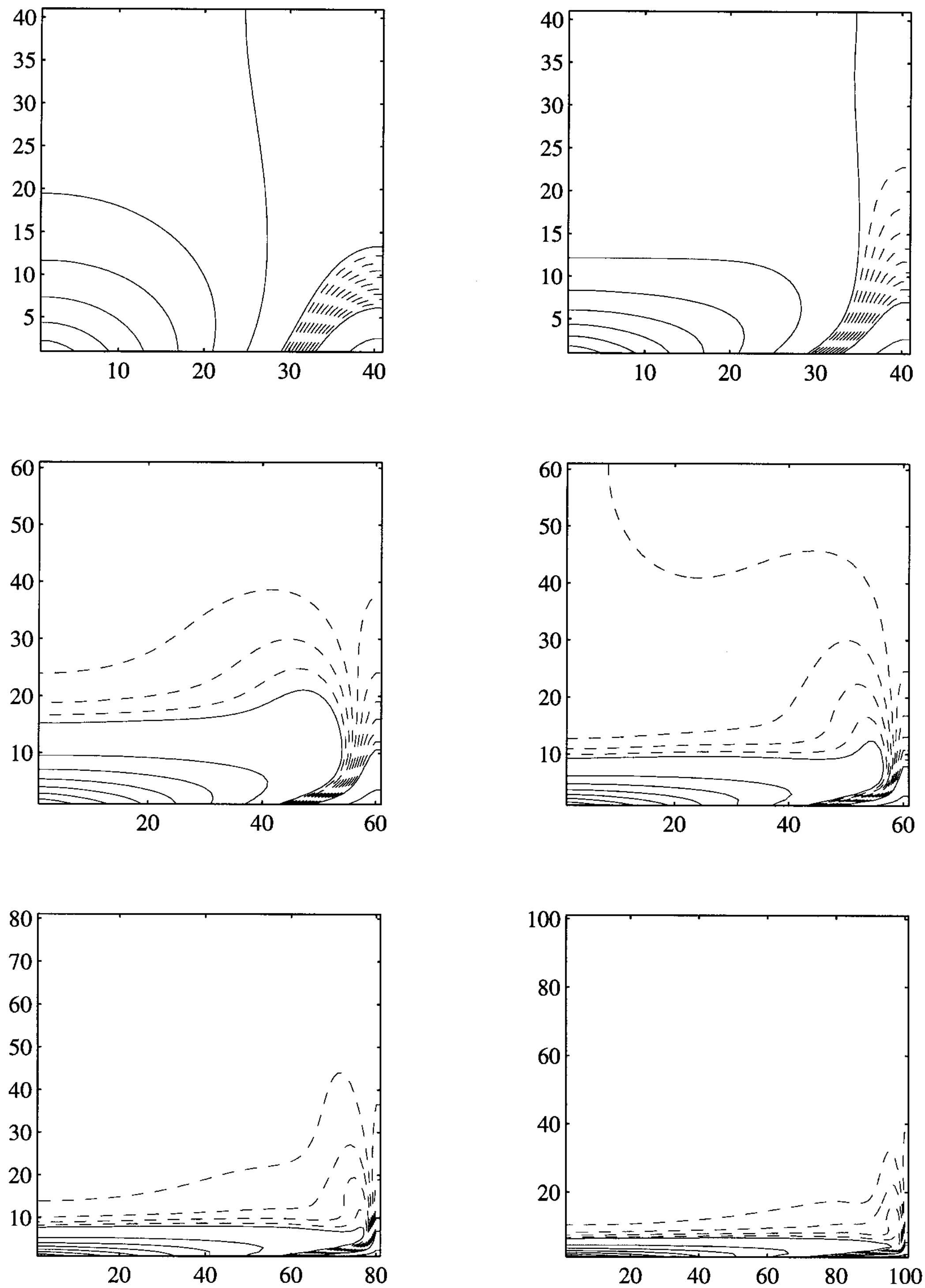

Fig. 2. $T(x, y)$ corresponding to the $\Psi(x, y)$ fields in Fig. 1. The axes indicate the number of grid points in the horizontal vertical. See Table 1 for further details.

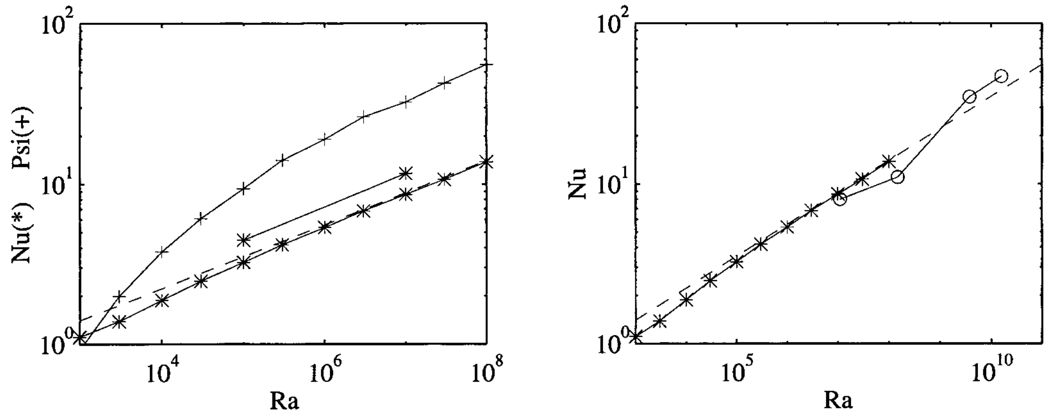

Fig. 3. Left panel: Ψ_{max} and Nu plotted as a function of Ra. The line between $Ra=10^5$ and $Ra=10^7$ is for the case $d=0.3$ in Table 3. Right panel: Nu(Ra) together with the experimental results from Rossby (1965).

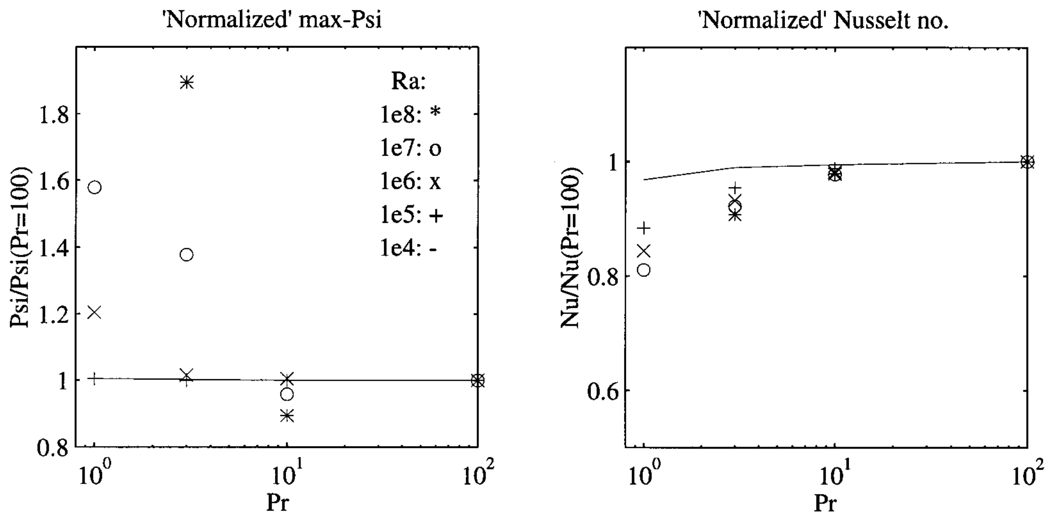

Fig. 4. Ψ_{max} and Nu normalized by their values at $Pr=100$ as a function of Prandtl number for Rayleigh numbers between 10^4 and 10^8 as indicated by the symbol table in the left panel.

Table 2. *Ψ_{max} and Nu as a function of Pr (across) and Ra (down)*

	Ψ_{max}				Nu			
	1	3	10	100	1	3	10	100
10^4	3.79	3.78	3.77	3.77	1.83	1.87	1.88	1.89
10^5	9.46	9.41	9.40	9.41	2.90	3.13	3.24	3.28
10^6	22.9	19.3	19.1	19.0	4.61	5.09	5.36	5.46
10^7	53.5	47.0	32.5	33.9	7.16	8.14	8.63	8.83
10^8		118	55.7	62.3		12.8	13.8	14.1

increasing. Nu decreases monotonically as Pr is decreased. (The $Ra = 10^8$, $Pr = 3$ case took extremely long to equilibrate; for this reason the $Pr = 1$ case was not considered.) Fig. 5 shows the stream function fields corresponding to Table 2. Confirming the observational fact that R65 obtained what appeared to be stable convection patterns at all Ra, a scale analysis shows why. Given that Ψ is non-dimensionalized by κ, it follows that we can write $\Psi_{max} = Pe$ where Pe is the Peclet number (UL/κ). The Reynolds number, UL/ν, is therefore Ψ_{max}/Pr, which is readily estimated. For the bottom left panel in Fig. 5, Re is ≈ 40. In the R65 experiments, the maximum Reynolds number (at $Ra = 1.6 \times 10^{10}$ and $Pr = 13$) would have been ≈ 12 (by extrapolating Ψ_{max} from $Ra = 10^8$).

There is a conspicuous qualitative change to the stream function field for $Pr < 10$ at high Ra. The center of the circulation shifts up and to the left. In fact, for $Ra = 10^8$ and $Pr = 3$ the circulation becomes quite intense and all but symmetric except for an increasingly complex boundary layer structure. Curiously, the mean temperature of the fluid is essentially independent of Pr (about 1% less at $Pr = 1$ than at $Pr = 100$).

At low Ra ($< 10^5$) the convection reveals only weak Pr dependence indicating that the nonlinear terms in (1) are negligable. At large Ra the Pr independence is limited to $Pr = 10$ and higher. At lower Pr Ψ_{max} increases substantially while the efficiency of heat transfer decreases compared to the $Pr = 10$ case.

3.2. *Experiments with non-linear temperature distribution*

The purpose of adjusting the temperature distribution, for the same total difference, is to

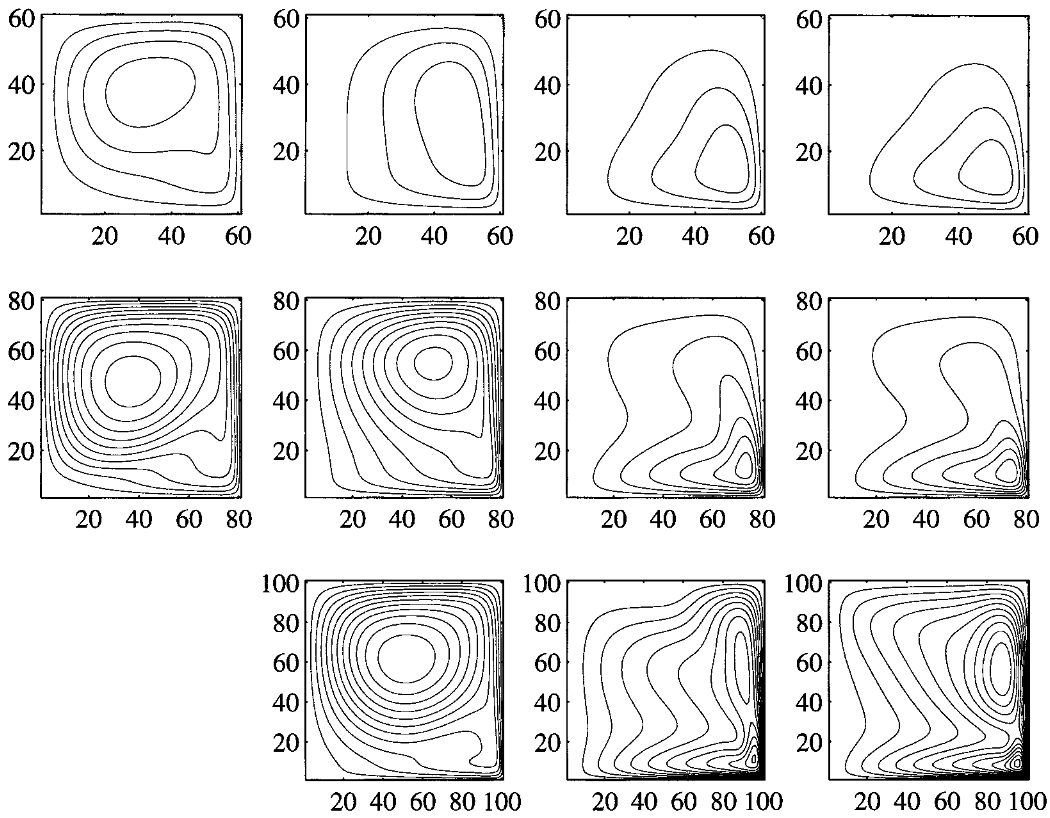

Fig. 5. $\Psi(x, y)$ fields corresponding to the Pr-Ra cases in Table 2. Increasing Pr (1, 3, 10, 100) to the right and increasing Ra (10^6, 10^7, 10^8) down. The axes indicate the number of grid points used. In all cases the contour interval is 5.

simulate the effect of different meridional density distributions. To keep the experiments simple and limited in number, we define the following function:

$$T(x) = \frac{\tanh((x - x_c)/d) - \tanh(-x_c/d)}{\tanh((1 - x_c)/d) - \tanh(-x_c/d)}, \qquad (13)$$

where T increases monotonically from 0 to 1 for $0 \leqslant x \leqslant 1$. For $d \gg 1$, $T(x)$ approximates a straight line. For temperature gradients > 1 at $x = x_c$, (13) is used to define the temperature at the bottom. For gradients < 1 at $x = x_c$, we use the same function, but reflected about $T(x) = x$. This is done by switching x and T: $x \rightarrow T$ and $T \rightarrow x$ as can be seen in Fig. 6, which shows the different temperature profiles used. The results are summarized in Table 3.

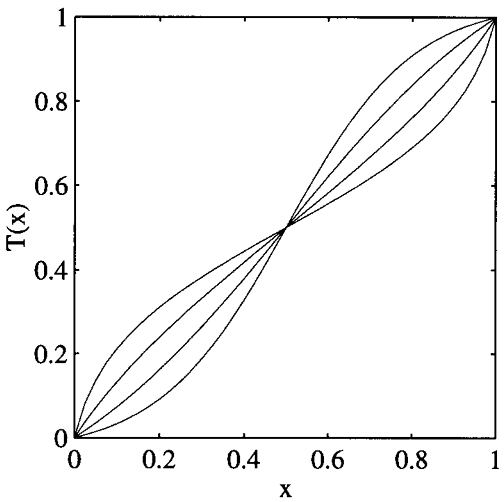

Fig. 6. Four different 'non-linear' temperature profiles imposed along the bottom (see text for details).

The more the temperature contrast is concentrated to the central part of the bottom (as indicated by $\mathrm{d}T/\mathrm{d}x$ at $x = x_c$ in Table 3), the longer a fluid parcel is subject to high temperatures before ascending into the interior. This leads to higher interior temperature and increased efficiency of heat transfer, as indicated by the increasing $\langle T \rangle$ and $H(d)/H(\infty)$ with decreasing d. Similarly, longer exposure along the cold half improves the removal of heat. The strength of the convection, as indicated by $\Psi_{\max}(\mathrm{d})/\Psi_{\max}(\infty)$, is much less affected by the shape of the imposed temperature.

The transient response of the system to a change in $T(x)$ is instructive. If the heating area increases so that $\langle T \rangle$ increases (going up in Table 3), the approach to final equilibrium is straightforward, i.e. warmer fluid penetrates into the interior by spreading out from the ascending plume along the right wall. If a decrease in $\mathrm{d}T/\mathrm{d}x$ is imposed (again for the same overall Ra), the ascending fluid is cooler than the interior and thus cannot penetrate to the top. As a result a second, frictionally driven cell of opposite sign appears on top of the thermal cell. This cell will shift to the upper left corner and slowly weaken while losing its remaining buoyancy through diffusion (see example next section).

In the following experiments, we limit ourselves to $\mathrm{Ra} = 3 \times 10^5$ and $\mathrm{Pr} = 10$. The reason for this choice is to work at a sufficiently high Ra where both $\Psi_{\max}$ and Nu follow the $\mathrm{Ra}^{1/5}$ power law indicating that the boundary layers are fully developed for both the momentum and density fields. Working at a higher Ra would require additional computer time for convergence. (All calculations were performed with MatLab v4.2c on a Macintosh powerPC.)

Table 3. *Effect of different temperature distributions at $Ra = 10^6$ on the circulation and heat transport relative to the linear profile case*

d	$\mathrm{d}T/\mathrm{d}x$ $(x = x_c)$	$\Psi_{\max}(d)/$ $\Psi_{\max}(\infty)$	$H(d)/H(\infty)$	$\langle T \rangle$	% err
0.3	1.79	1.05	1.35	0.768	2.5
0.6	1.22	1.05	1.12	0.730	6.6
∞	1.0	1.00	1.00	0.716	6.6
0.6 (switched)	0.819	0.94	0.88	0.702	6.5
0.3 (switched)	0.559	0.86	0.67	0.663	7.8
0.3 ($\mathrm{Ra} = 10^5$)	1.79	1.11	1.38	0.746	2.0
0.3 ($\mathrm{Ra} = 10^7$)	1.79	1.08	1.35	0.786	3.6

3.3. *Slightly non-antisymmetric temperature boundary conditions*

The purpose here is to investigate the transient response of the convection to a slight change in thermal forcing, either at the warm end or at the cold end. To keep the experiment simple, the temperature profile is adjusted by breaking the linear temperature profile into three linear segments. Two cases represent a perturbation along the cold half such that the temperature profile is slightly warmer (a) or slightly colder (b), while the imposed temperature between 0.5 and 1 is kept unchanged. The other two cases represent change along the warm half, either slightly warmer (c) or colder (d), while keeping the temperature between 0 and 0.5 unchanged, Fig. 7.

All 4 cases are initialized with the equilibrium solutions with a linear temperature profile for $\mathrm{Ra}=3\times10^5$, Fig. 8 (upper panels). The shape of the resulting equilibrium temperature and streamfunction fields are quite similar and are not shown. More interesting is the fluid's temporal response to the new boundary conditions and resulting mean temperature. If a change is imposed at the warm end (cases (c) and (d) in Fig. 7), the perturbation will be communicated by the ascending fluid throughout the interior, whereas a change at the cold end is quickly 'forgotten' as the fluid parcel sweeps past the warm unaltered segment such that there is little change in mean temperature. This emphasizes what is intuitively obvious, namely that the interior temperature will be set by the temperature of the fluid just prior to leaving the active boundary. It also follows that if a change is imposed at the warm end, the time required to adjust the interior volume will take a long time whilst a change at the cold end (cases (a) and (b) in Fig. 7) involves only the bottom boundary layer and is accordingly much more rapid. This brings out an important point, namely that the heat transport involves two components, a slow path through the interior and a fast path along the bottom boundary layer. Fig. 9 shows the heat flux imbalance during the four adjustments to equilibrium. The grouping of the four panels correspond to the four temperature profiles in Fig. 7: the upper panels show the response to added heating at the cold (a) and warm ends (c), while the lower panels (b and d) show the corresponding responses when additional cooling is imposed. The number in the upper right hand shows the resulting mean temperature, $\langle T\rangle$. The adjustment takes much longer when the perturbation is imposed at the warm end than at the cold, regardless if the effect is to raise or to lower the bottom temperature, upper and lower panels, resp. The longest adjustment is when the temperature is dropped slightly at the warm end (case (d)). In this case the slightly cooler ascending fluid can no longer penetrate to the top and a frictionally driven secondary cell develops, Fig. 8 (lower left panel), the strength of which is about one-tenth that of the convectively driven cell. The corresponding temperature plot shows only a very weak temperature range of 0.005 units. Consistent with the long cooling time, the percent error in Nu is only a few percent negative. This case had to be run about $5\times$ the time plotted in Fig. 9 to reach the equilibrium heat flux error of $\sim 6\%$. (A smaller error could have been obtained by running the model at higher resolution, at the expense of computer time.) In summary, it takes a long time for a perturbation at the warm end to bring the enormous reservoir of the interior to a new equilibrium, whereas a perturbation of the stratified boundary layer is rapidly adjusted to.

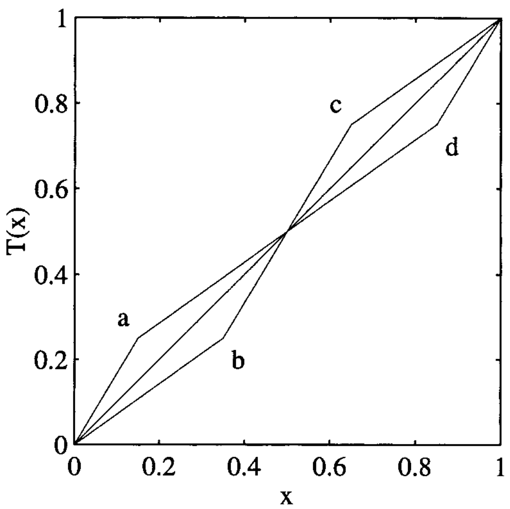

Fig. 7. Four different temperature perturbations to the linear profile to simulate slightly non-antisymmetric conditions (see text for details).

3.4. *Effect of a pseudo-Ekman mode*

The ocean circulation is driven not only thermally, but also mechanically. In the subtropics,

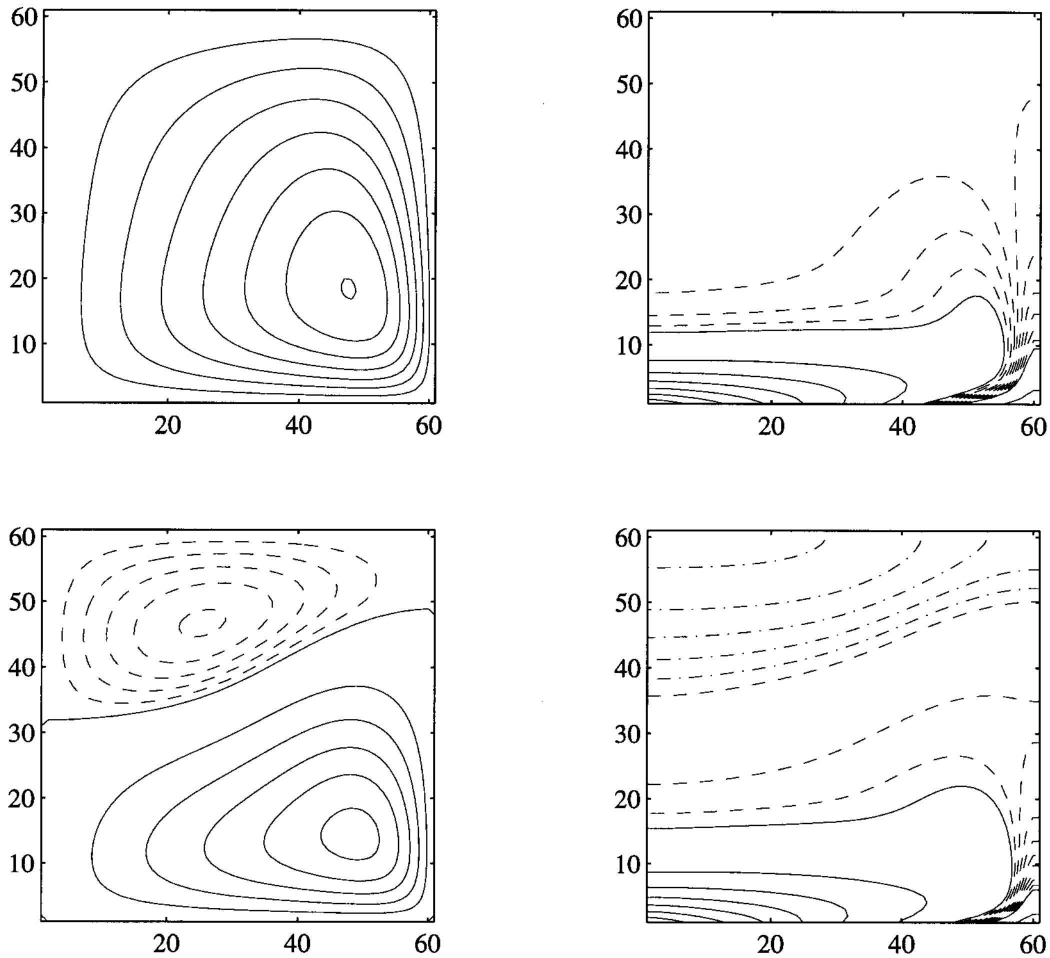

Fig. 8. Upper panels: equilibrium $\Psi(x, y)$ and $T(x, y)$ fields at $\mathrm{Ra}=3\times10^5$, $\mathrm{Pr}=10$ with a linear temperature profile along the bottom. Lower panels: $\Psi(x, y)$ and $T(x, y)$ fields after 1200 steps (non-dim. time = 0.056; see Fig. 9), forced with temperature profile (d) in Fig. 7. The $\Psi(x, y)$ field ranges from 10.7 to -1.03 in the secondary cell. The contour interval is 2 in the positive region and 0.2 (dashed lines) in the secondary cell. The contour interval for T is 0.1 and 0.01 (between 0.7 and 0.8) and 0.001 units in the region of the secondary cell.

the Ekman convergence at the surface causes a downwelling that pushes the thermocline some 400–800 m below the surface depending upon latitude. This associated 3-dimensional circulation is of course intrinsically linked to the rotation of the planet, which we cannot incorporate in this model. However, we can simulate the up- and downwelling by imposing a vertical velocity at the bottom boundary while maintaining the linear temperature boundary condition. In this sense, an inflow in the cold half and outflow in the warm half would represent the downwelling of warm water in the subtropical and upwelling in the subpolar gyre. This approach differs from BF72 who imposed a stress along the bottom. There are two reasons for trying this approach instead. First, by imposing a vertical velocity the thermal boundary layer will separate from the bottom and generate an internal thermal boundary, i.e., a 'thermocline'. This did not happen for the case considered by BF72. Second, the strength of this mechanical forcing is readily expressed in terms of a stream function which can be directly related to the interior stream function resulting from the thermal forcing.

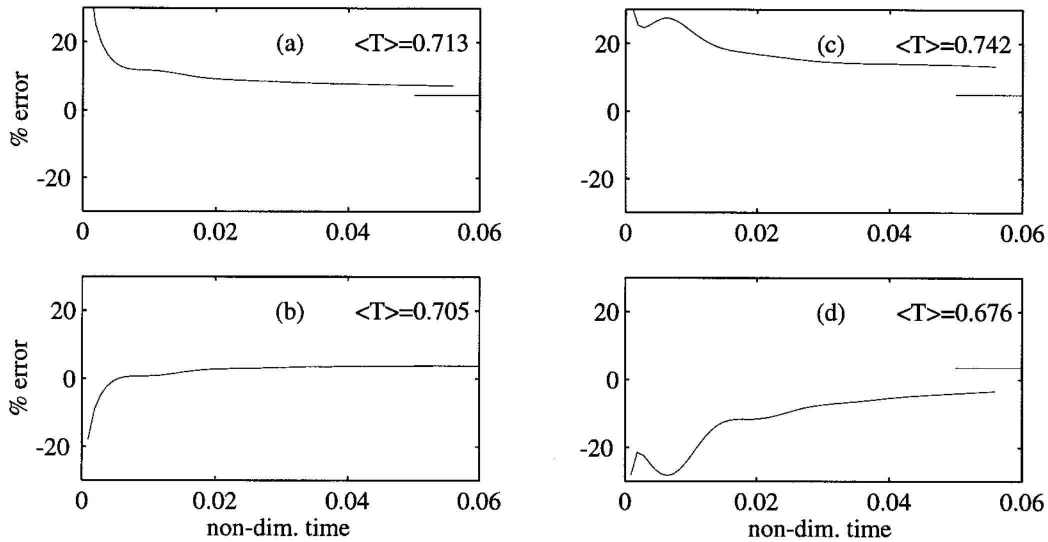

Fig. 9. Heat flux imbalance during adjustment to equilibrium for four cases of localized heating or cooling corresponding to the altered temperature profiles in Fig. 7. The timescale is non-dimensionalized by L^2/κ ($\mathrm{Ra}=3\times10^5$).

The question, then, is how this externally imposed pumping modifies the structure of the convection. On the one hand, where fluid is pumped in, the thermal boundary layer will separate from the bottom thereby weakening the heat transfer to/from the interior. On the other hand, this pumped mode represents a forced convection in its own right which will get modified by the thermal mode. If there is no thermal forcing at all, a simple symmetric circulation will result reflecting the symmetric forcing, Fig. 10. The imposed in- and outflow is expressed as a simple sine function along the bottom boundary: $\Psi_b=\Psi_o\sin(\pi x)$, where $0<x<1$ as before. Ψ_o is varied such that the resulting circulation can be compared to the purely thermal case. The free-slip boundary conditions remain unchanged.

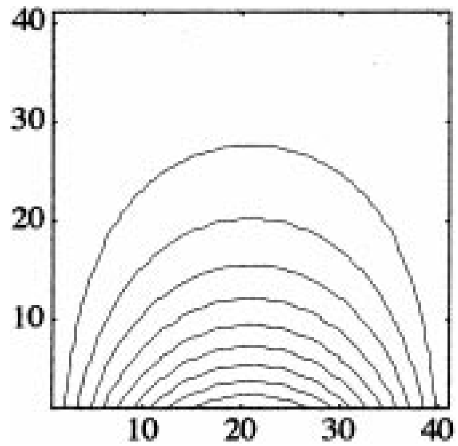

Fig. 10. $\Psi(x, y)$ for an imposed Ψ_b along the bottom without thermal forcing, i.e., $\mathrm{Ra}=0$. The axes indicate the horizontal and vertical gridpoints.

It is not possible to define Nu as we have used it above. The reason is that we have a mass flow through the system that has to be closed externally. One resolution to this would be to include an outside return flow, which one could think of as a 'pseudo-Ekman' layer but to belabor this would be to push the analogy too far. Since the properties of this return flow are not solved for, its contribution to the heat flux cannot be determined. We therefore limit ourselves to a qualitative inspection of the strength and shape of the resulting circulation and temperature fields as a function of the combined thermal and mechanical forcing, Table 4.

The resulting stream function and temperature fields for two cases are shown in Fig. 11. The upper panels shows the stream function and temperature fields for $\Psi_o=-10$ (suction at warm end) while the lower panels correspond to $\Psi_o=10$ (suction at cold end). In the first case the interior $\Psi=0$ streamline separates the interior

Table 4. *Ψ_{max} and $\langle T \rangle$ as a function of Ψ_o ($Ra = 3 \times 10^5$, $Pr = 10$)*

Ψ_o	Ψ_{max}	$\langle T \rangle$	N
−10	15.5	0.48	81
−5	14.3	0.62	81
0	14.1	0.71	61
5	13.0	0.78	81
10	13.1	0.82	81

from the bottom everywhere. The temperature ranges from 0.2 to >0.9 along the interior $\Psi = 0$ across which there is no advection. In the stratified region $(\partial T/\partial y)_{max}$ coincides with $\Psi = 0$ whereas towards the warm end $\partial T/\partial y$ turns strongly negative along $\Psi = 0$ reflecting the diffusive heat flux into the interior. (The locus of maximum stratification or 'thermocline', the dashed line in Fig. 11 (upper right panel), penetrates deeper into the interior and weakens.) The variation in Ψ_{max} is modest compared to that of Ψ_o suggesting that the interior cell is still driven significantly by thermal diffusion, in this case by an interior boundary layer instead of one along the bottom. For the opposite case ($\Psi_o > 0$) the forced and thermally driven cells combine together leading to much higher interior temperature while the stream function weakens because the circulation is increasingly driven mechanically and not by buoy-

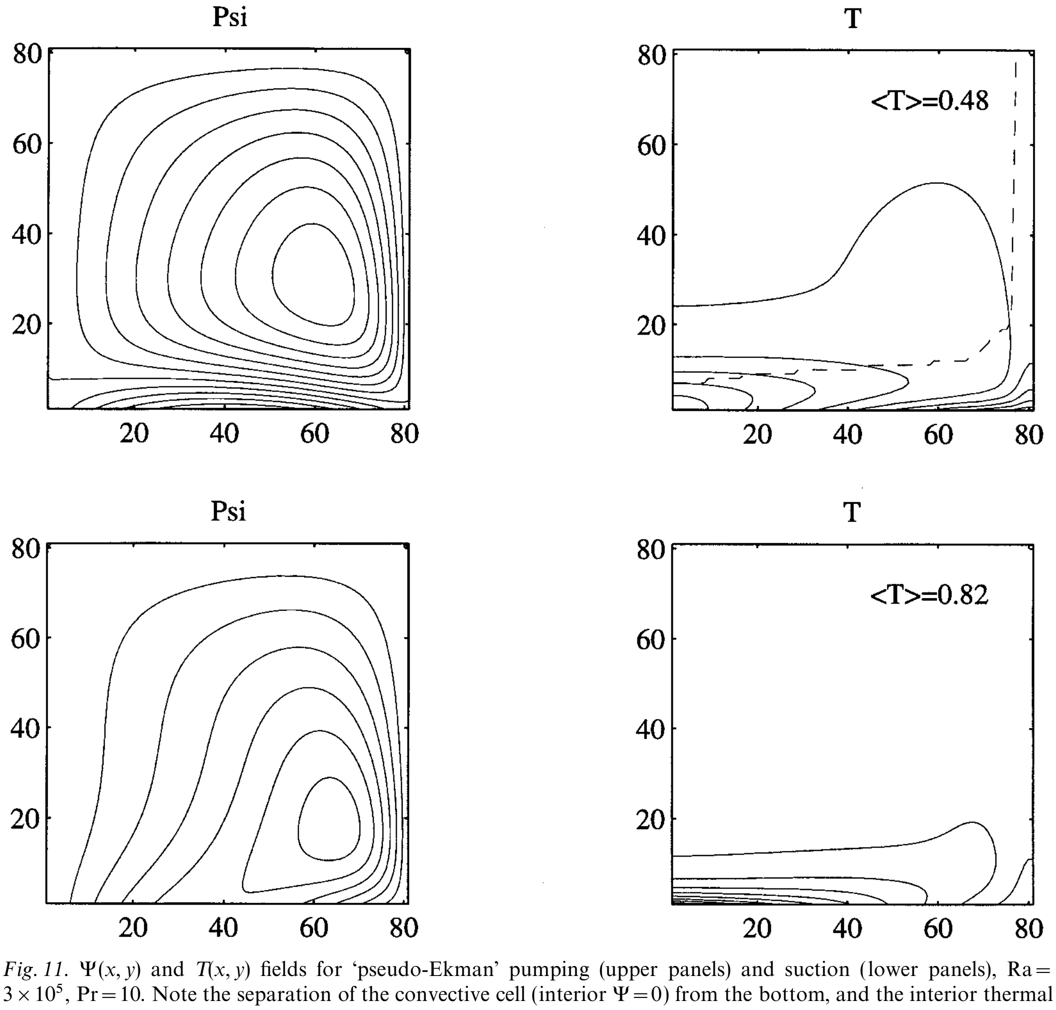

Fig. 11. $\Psi(x, y)$ and $T(x, y)$ fields for 'pseudo-Ekman' pumping (upper panels) and suction (lower panels), $Ra = 3 \times 10^5$, $Pr = 10$. Note the separation of the convective cell (interior $\Psi = 0$) from the bottom, and the interior thermal boundary layer (or thermocline) indicated by the dashed line. Contour interval in both cases is 2.

ancy. The very thin thermal boundary layer in the lower right panel of Fig. 8 would be our nearest analogue to a shallow subpolar thermocline where by definition Ekman suction predominates.

4. Discussion and summary

The most important conclusion of this study is that the rate of convection is a definite but weak function of the imposed thermal gradient. Nu is proportional to $Ra^{1/5}$, and at high Ra Ψ_{max} tends to the same power law. This agrees with the scale analysis and experimental results of R65. Due to machine limitations the earlier numerical study by BF72 was limited to modest Ra (3×10^5). They report a $Ra^{0.36}$ dependence for Ψ_{max}, but it is also clear from their Fig. 3 and our Fig. 3 that their Ψ_{max} had not yet reached asymptotic form. Their Nu estimates show asymptotic behavior starting at $Ra > 10^4$, similar to what we find, but with a power of 0.25 compared to our 0.2. The difference is not large, and may be attributed to the limited Ra range together, possibly, with their zero velocity instead of our free-slip boundary condition at the sides and top.

The numerical agreement between these calculations and the experimental results of R65 is unexpectedly good. In Fig. 3 (right panel) the Nu estimates from R65 are superimposed on the results from this study. The asymptotic behavior is clear, but the degree of numerical agreement in the values of Nu is surprising. First, this study uses free-slip boundary conditions compared to the zero velocity conditions in the experiments. Second, as pointed out in R65, the Nu estimates may be a bit high due to the finite size of the thermistor sensors used to determine the temperature gradient in the boundary layer. In addition, the experiments were conducted in a tank with an aspect ratio of 2.5 : 1.

Consistent with all earlier studies, we find that the mean temperature is only a very weak function of Ra. At the same time the interior temperature and heat flux are very sensitive to the shape of the imposed temperature profile. For different temperature distributions, we find that while the Ra dependence is still the same (1/5 power law), Nu can differ by a factor two. The sharper the transition from cold to warm, the longer a parcel is exposed to the extreme temperature in the boundary layer. Once a parcel leaves the boundary it carries this thermal imprint into the interior. The significance of these results is that given any non-uniform temperature distribution a convective cell will develop. It is not the ascending warm fluid that 'drives' the rest of the circulation, it is the imposed temperature gradient (last term in eq. (1)) that puts the fluid along the bottom in motion, draws fluid from the interior above and returns it to the interior in a narrow convective plume. The asymmetry results from the relative inefficiency of conduction (cooling of the fluid as it approaches the bottom) compared to the convective warming of the interior. There is no stability issue here as with Benard convection.

Experiments with small changes in thermal forcing emphasize a point worth remembering, namely that the net heat flux is made up of two components or branches, a direct path along the boundary and the long path through the interior. This becomes evident from the system response time when the fluid is subject to a change in thermal forcing, depending upon where the perturbation is imposed. If it occurs where the fluid is highly stratified, the perturbation is rapidly communicated along the boundary layer and its memory is lost in the advective-diffusive adjustment in the boundary layer. If it occurs at the convecting end, the change is transmitted to the interior with the result that much more time is required to reach a new equilibrium. This is illustrated in Fig. 9, which shows the error in heat flux (or the heat flux divergence necessary to bring the fluid to its new equilibrium).

5. Oceanographic implications

The very simple convection experiments reported here, non-rotating, two-dimensional, and limited to steady-state solutions, were, as discussed in the introduction, motivated by the striking asymmetry in area between the limited regions of sinking versus the broad expanse of presumed upwelling everywhere else (presumed only because upwelling is not directly measureable). As such they represent extreme idealizations of the large thermohaline overturning of the oceans. While mindful of these simplifications, it is of interest to assess them in an oceanographic context.

Over the latitude range (0–55°N) that the North Atlantic and North Pacific have in common (i.e., deep water) the meridional density contrasts at the surface are comparable to each other, 4–5 kgm^{-3} (Levitus, 1982). Thus, one might conclude that the corresponding thermohaline overturning should be of a similar magnitude, and insofar as intermediate water production is concerned this appears to be the case. In the North Atlantic, the Labrador Sea waters (8.5×10^6 m^3 s^{-1}; McCartney and Talley, 1984) appear to spread along two pathways: eastward across the Mid-Atlantic Ridge, and south inshore and under the North Atlantic Current. In the North Pacific, the North Pacific Intermediate Waters (7×10^6 m^3 s^{-1}; Talley et al., 1995) at first spread south along the continental margin, and then to the east, of which about 3×10^6 m^3 s^{-1} spread out within the lower thermocline of the subtropical gyre (Talley et al., 1995). While these intermediate water masses do not join the global abyssal circulation, they do form a thermohaline mode. Where the North Atlantic differs is that it has another major source which has no counterpart in the Pacific, namely a 5.6×10^6 m^3 s^{-1} shallow overflow into the deep North Atlantic between Scotland and Greenland (Dickson and Brown, 1995). These waters flow obliquely to greater depths, along which they entrain intermediate depth and Labrador Sea waters resulting in a transport of North Atlantic Deep Waters (NADW) at Cape Farewell of $\sim 13 \times 10^6$ m^3 s^{-1}, more than twice that due to the overflow alone. These NADW are subsequently steered by topography south along the deep western margin of the ocean. As such, this deep component of the thermohaline overturning has a rather two-dimensional character: the upper limb of the thermohaline mode is a swift western boundary current: the Florida Current-Gulf Stream-North Atlantic Current-Subpolar Front sequence while the lower limb has a direct meridional path (the deep western boundary currents) back to the south.

The fundamental difference between intermediate and bottom water spreading is therefore that the former are constrained to spread zonally along lines of constant planetary vorticity due to blocking by the separated western boundary currents whereas the latter are guided by deep topographic gradients (i.e. meridionally along the continental rise). It is not a lack of production but the rotational constraint that acts to limit the intermediate waters to the basins in which they were formed.

In summary, the thermohaline circulations depend upon the poleward density gradients at the surface for their existence, not the convection at high latitudes per se. The convective overturning takes place whereever the stratification is weakest. How deep the waters sink depends upon the density of the convecting fluid relative to the underlying waters. Those waters that reach the bottom will be those that spread out to the World Ocean along the deep western margins to supply the interior upwelling necessary to replace the poleward moving waters of the upper ocean (Stommel and Arons, 1960).

6. Acknowledgments

Dr. Hyun-Sook Kim spared me much trouble by having available a Poisson solver written in MatLab. Dr. Clark Rowley suggested several improvements to the code to save computer time. Much of this work was done during an invitation to the newly formed Physical Oceanography group at the University of Stockholm, headed by Prof. Peter Lundberg. The hospitality and friendliness of Professor Lundberg and his colleagues is very much appreciated. It is my pleasure to thank Professor George Veronis for a careful reading of the manuscript and making several welcome suggestions for its improvement. I would also like to thank the editor and two reviewers for very helpful comments on the text.

REFERENCES

Arakawa, A. 1966. Computational design for long-term numerical integration of the equations of fluid motion: Two-dimensional incompressible flow. Part 1. *J. Comput. Phys.* **1**, 119–143.

Beardsley, R. C. and Festa, J. F. 1972. A Numerical Model of convection driven by a Surface Stress and Non-Uniform Horizontal Heating. *J. Phys. Oceanogr.* **2**, 444–455.

Dickson, R. R. and Brown, J. 1994. The production of north Atlantic deep water: sources, rates and pathways. *J. Geophys. Res.* **99(C6)**, 12319–12341.

Levitus, S. 1982. *Climatology of the ocean.* NOAA Prof.

publ. #13. U. S. Government Printing Office. Washington, D. C.

McCartney, M. S. and Talley, L. D. 1984. Warm-to-cold water conversion in the northern north Atlantic Ocean. *J. Phys. Oceanogr.* **14**, 922–935.

Press, W. H., Flannery, B. P., Saul Teukolsky and William Vetterling 1986. *Numerical recipes: the art of scientific computing*. Cambridge Univ. Press. 818 pp.

Rossby, H. T. 1965. On thermal convection driven by non-uniform heating from below: an experimental study. *Deep Sea Res.* **12**, 9–16.

Somerville, R. C. 1967. A non-linear spectral model of convection in a fluid unevenly heated from below. *J. Atmos. Sci.* **24**, 665–676.

Stommel, H. 1962. On the smallness of the sinking regions in the ocean. *Proc. Natl. Acad. Sci.* **48**, 766–772.

Stommel, H. and Arons, A. B. 1960. On the abyssal circulation of the world ocean (II). An idealized model of the circulation pattern and amplitude in oceanic basins. *Deep-Sea Res.* **6**, 217–233.

Talley, L. D., Nagata, Y., Fujimura, M., Imao, T., Kono, T., Inagake, D., Hirai, M. and Okuda, K. 1995. North Pacific Intermediate water in the Kuroshio/Oyashio mixed water region. *J. Phys. Oceanogr.* **25**, 475–501.